Chapter 4

The Local Structure of SOFC Materials Investigated by X-Ray Absorption Spectroscopy

Antonino Martorana,[a] Francesco Giannici,[a] and Alessandro Longo[b]

[a]*Dipartimento di Fisica e Chimica, Università di Palermo, viale delle Scienze, 90128 Palermo, Italy*
[b]*ISMN-CNR, via Ugo La Malfa, 153, 90146 Palermo, Italy*

antonino.martorana@unipa.it

This chapter is devoted to the analysis of the local atomic structure of solid oxide fuel cell (SOFC) electrolyte and electrode materials. Among the experimental techniques able to provide information about the local structure of materials, the X-ray absorption spectroscopy has the peculiarity of element selectivity, allowing to investigate the chemical environment of specific atoms embedded in a matrix. Solid oxide electrolytes allow the conduction of ionic charge carriers between the electrodes of a SOFC device; the mechanism of ion conduction depends on the type of carrier, and it is finely tuned—or even only possible—if the solid matrix is suitably tailored by insertion of doping species that modify the local structure and the dynamics of the lattice. The oxygen

Structural Characterization Techniques: Advances and Applications in Clean Energy
Edited by Lorenzo Malavasi

ISBN 978-981-4669-34-4 (Hardcover), 978-981-4669-35-1 (eBook)
www.panstanford.com

reduction and fuel oxidation processes are catalyzed at the respective electrodes; moreover, the cathode and anode layers must: (1) allow an efficient exchange of reactants with the environment, (2) convey the ionic species to/from the electrolyte and (3) ensure the conduction of the electrons involved in the reduction and oxidation processes. The chemical and physical stability of the interface with the electrolyte layer is another essential issue of electrode materials. The chapter begins with a section describing the basic theory underlying the X-ray absorption spectroscopy and the experimental set-ups used in fuel cell applications. The second section reports on case studies and perspectives of future development of fuel cell materials under the keynote of local structure.

4.1 X-Ray Absorption Spectroscopy

X-Ray Absorption Spectroscopy (XAS) is an atomic absorption spectroscopy. In the following paragraph, we will see how it is used to gain insights on the local atomic structure of a single element in a solid oxide. Different acronyms are used in the literature to refer to XAS techniques. These are EXAFS—extended X-ray absorption fine structure, the oscillations of the XAS spectrum far from the absorption edge; XANES—X-ray absorption near-edge structure, the features of the XAS spectrum superimposed on the absorption edge; XAFS—X-ray absorption fine structure, comprising both XANES and EXAFS. Let us consider a monochromatic beam of hard X-rays (with energy 5–50 keV) interacting with a ceramic oxide (e.g., CeO_2, or $Y:BaZrO_3$).[1] The X-ray interaction with matter in this case is dominated by photoelectric absorption: when the energy of the impinging photons is larger than the binding energy of a core electron, this is ejected to the continuum (photoelectron). The intensity of the

[1]We restrict here to the case that is most relevant for SOFCs, while XAS can be employed on glassy, liquid or gaseous samples, and is not restricted to hard X-rays. However, the data analysis scheme presented here is valid for hard X-rays only. Soft X-rays, used for the analysis of lighter atoms, involve completely different experimental setup and data analysis models: moreover, the information contained in the XAS spectra of lighter elements (for which the term NEXAFS, Near Edge XAFS, is often used) mainly concerns the electronic structure rather than the atomic structure.

incoming and transmitted beams is labeled I_0 and I_1, respectively. The X-ray absorption coefficient of a sample of thickness x, defined as

$$\mu = \frac{1}{x} \ln \frac{I_0}{I_1}, \tag{4.1}$$

decreases smoothly with increasing energy (the X-rays being more penetrating as their energy grows), until the energy matches the binding energy of a core electron: At this point, the absorption coefficient rises accordingly. The sudden increase of μ as a function of E is called the absorption edge.

This is not different from other absorption spectroscopies: In particular, since the X-ray energy is high, the photons are able to excite electrons from core states, which are atomic rather than molecular. Therefore, the transition energy is defined only by the atomic species rather than by bonding or oxidation state. In conclusion, XAS is an atomic spectroscopy like AAS or XPS: A single element can be probed selectively by tuning the radiation energy in order to match the energy of the atomic transition, regardless of the oxidation state, coordination environment, or spatial distribution within different phases. This is the first main feature of XAS: Using the right X-ray energy it is possible to focus on one atomic species at a time (e.g., X-rays of 19 keV only excite the 1s electrons of niobium, see Fig. 4.1).

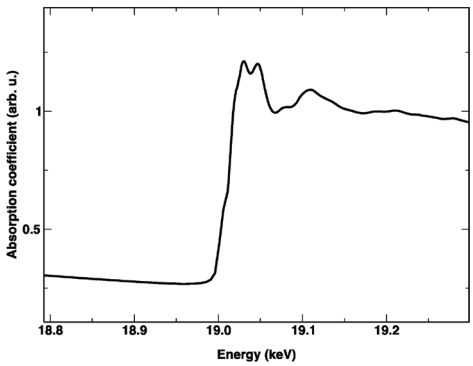

Figure 4.1 An X-ray absorption spectrum around the K-edge of niobium (19 keV).

The transition of a core electron to the continuum is labeled using letters, so that the ejection of a 1s electron is called K edge,

2s is called L_1 edge, and 2p electrons give rise to the L_2 and L_3 edges.[2] The hard X-ray range covers approximately the K edges of elements heavier than Sc, and also the L edges of heavier elements, from about Sn onwards. For the heaviest elements (lanthanides and beyond), the K edges lie at very high energies (40–80 keV), which present experimental difficulties: For this reason, the L edges of such elements are often used.

4.1.1 EXAFS Theory

The following is a simplified picture of the absorption process, and of the derivation of the relevant EXAFS equation that is used for quantitative data analysis. While this is only valid under certain assumptions, it is nonetheless useful to grasp the physical basis of XAS.[3]

The photoelectron coming off the absorber atom propagates as an outgoing spherical wave: for an isolated atom, the photoelectron does not interact with anything, and the XAS spectrum is smooth (this absorber-only atomic contribution, μ_0, is of pivotal importance in data analysis). The fine-structure modulation of the absorption is the result of the quantum interference of the photoelectron wave with itself, after interacting with the atoms around the absorber.

It is possible to derive the EXAFS oscillations quantitatively from first principles, under certain assumptions that are only met outside of the near-edge region.[4] As the outgoing wave impinges with a neighboring atom, it is scattered back as an incoming wave that interferes with the outgoing wave (like the ripples on water hitting the border of a pond).

Since the interatomic distance is fixed, the interference of the waves is alternately constructive and destructive as a function of the photoelectron wavevector **k**, as defined by the following relation:

---

[2]Due to spin-orbit splitting into $2p_{1/2}$ and $2p_{3/2}$. The sequence of edge energies is $L_3 < L_2 < L_1 < K$.

[3]Thorough treatments of EXAFS theory are presented in the classical works by Teo [1] and Stern [2] and were reviewed by Rehr and Albers [3]. A recent primer to the topic is [4].

[4]These are: (1) only one electron is ejected; (2) the X-ray wavelength is much larger than the core orbital; (3) the photoelectron energy is high enough that all the other electrons are frozen in place during the process.

$$k = \sqrt{(2m_e/\hbar^2)(E - E_0)} = \sqrt{0.263(E - E_0)}, \quad (4.2)$$

where E_0 is the edge position (i.e., the electron binding energy), and E the incoming beam energy. Therefore the $E - E_0$ term is the energy carried by the outgoing photoelectron. The second form of the equation is valid for the energy in eV and wavevector in Å, as it is customary. The relation between the interatomic distance and the constructive interference condition is shown in Fig. 4.2a, while destructive interference is represented in Fig. 4.2b. It can be demonstrated that the EXAFS fine structure equals the amplitude of this interference, and that it appears as an additional oscillatory contribution to the absorption coefficient plot.

Figure 4.2 (a) The outgoing wave (black) interferes constructively with the incoming wave (gray); (b) Changing the wavelength, the interference is now destructive.

The fine structure term features: (1) an oscillatory term that takes into account the constructive and destructive interference as a function of k; (2) a $1/kR^2$ term that comes from the spherical wave amplitude; (3) the overall amplitude and phase shift functions $F(\mathbf{k})$ and $\delta(\mathbf{k})$, that represent the quantum-mechanical process of ejection and backscattering. These functions arise from the interactions between photoelectrons and atoms, so they are determined by the nature of the absorber-backscatterer pair, and they carry the chemical information contained in the EXAFS spectrum. Amplitudes and phase shifts used to be measured from model compounds, but nowadays they are calculated with programs like FEFF or GNXAS for any given atomic configuration.

The contribution from each of the atoms in a coordination shell is additive, so N_i atoms in the i-th coordination shell, placed at distance R_i from the absorber, give rise to the EXAFS signal:

$$\chi(k) \propto \sum_i \frac{N_i F_i(k)}{kR_i^2} \sin(2kR_i + \delta_i(k)) \tag{4.3}$$

Further refinements of the model involve (1) the photoelectron mean free path, $\lambda(\mathbf{k})$; (2) the variance of the interatomic distance, σ^2, accounting for the static and vibrational disorder blurring the pair distribution function (often referred to as the Debye–Waller factor, although this should not be confused with the disorder factor of diffraction with the same name); (3) an overall amplitude parameter S_0^2 (slightly lower than unity) accounting for inelastic effects. In conclusion,

$$\chi(k) = S_0^2 \sum_i \frac{N_i F_i(k)}{kR_i^2} \sin(2kR_i + \delta_i(k)) e^{-2\sigma_i^2 k^2} e^{-2R_i/\lambda(k)} \tag{4.4}$$

that is the complete EXAFS equation in harmonic approximation. The main points to note are: (1) the $\mathbf{k}R^2$ term at denominator, and the limited mean free path of the photoelectron, restrict the range of the outgoing wave to about 6 Å in most cases; (2) the disorder severely dampens the signal at high k values, so that an ordered structure frozen at 20 K can have a good signal up to k = 25 Å^{-1}, but the spectrum of a glass or a crystal at high temperatures may fall off at about 10 Å^{-1}. This is the second main feature of XAS: it only probes the local environment of the absorbing atom, comprising a few coordination shells, and it is extremely sensitive to local disorder.

All of the above, derived for a single scattering event, can be generalized for every multiple scattering (MS) path between the absorber and any other group of neighboring atoms. MS paths are in general less important than single scattering, since they have lower $F(\mathbf{k})$ and higher σ^2, but they have to be taken into account especially in the following cases: (1) collinear arrangements of atoms, e.g., in symmetric structures like perovskite; (2) low k-values, where the disorder damping is less important.[5]

[5]MS can also arise between two atoms, if the photoelectron bounces back and forth more than once. The probability of this event is lower than single scattering but it can be significant nonetheless when modeling a spectrum quantitatively.

4.1.2 EXAFS Data Analysis

The experimental fine structure term is conveniently normalized so that it is independent on the total absorption of the sample:

$$\chi = \frac{\mu - \mu_0}{\mu_0} \tag{4.5}$$

The first conundrum of EXAFS analysis is that μ_0 (the isolated absorber contribution) cannot be measured, so it must be defined recursively as the total spectrum minus the fine-structure contribution from the neighboring atoms (while EXAFS is defined using μ_0 itself). The subtraction of the background (extraction) is arbitrary to a degree, and it is one of the pitfalls of the EXAFS analysis. In practice, μ_0 is approximated as a smooth function of E, while the oscillatory features are attributed to the interatomic correlations.[6] This may be better visualized and understood using the Fourier transform (FT). An EXAFS spectrum and the corresponding FT are shown in Fig. 4.3.

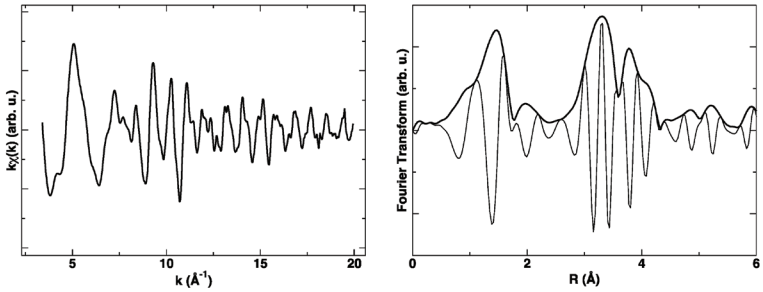

Figure 4.3 An EXAFS spectrum in k-space (left) and its Fourier Transform in R-space (right). The real part and the magnitude of the FT are plotted as thin and thick black lines, respectively.

The interatomic correlations contribute to the EXAFS signal with superimposing sinusoidal waves, and the frequency of each wave increases with the interatomic distance R. The Fourier transform can be employed on the $\chi(\mathbf{k})$ spectrum (vs. $Å^{-1}$) to

[6]A number of mathematical models have been proposed in the literature, most of them based on smoothing splines. More sophisticated approaches employ additional functions to reproduce multi-electron transitions appearing as smaller secondary absorption edges.

obtain a χ(R) spectrum (vs. Å), where each peak corresponds to a coordination shell, as a function of the distance from the absorber. In this way, the μ_0 background represents a low-frequency contribution placed at distances that cannot correspond to any neighboring atoms (i.e., R < 1 Å). By minimizing this low-R signal, one obtains the real EXAFS signal free from atomic contributions due to the absorber only. The different structural parameters all have direct effects on the height and shape of peaks in the FT plot: coordination number affects peak height, $F(\mathbf{k})$ affects the peak shape, disorder affects peak width, and distance controls the peak position.

Since the single components are weighted by $F(\mathbf{k})$, a simple qualitative analysis of the FT is not feasible, especially when MS is relevant. For this reason, a multiparametric least-square fitting is commonly used to extract the structural parameters from the spectra. Sophisticated data analysis methods have been described in the literature, but they are far outside the scope of this introduction.[7]

Choosing a reasonable model, and finding the global minimum in the parameter space is a difficult task. Model fitting is carried out with minimization algorithms, usually providing also a graphical insight into the model suitability (Fig. 4.4).

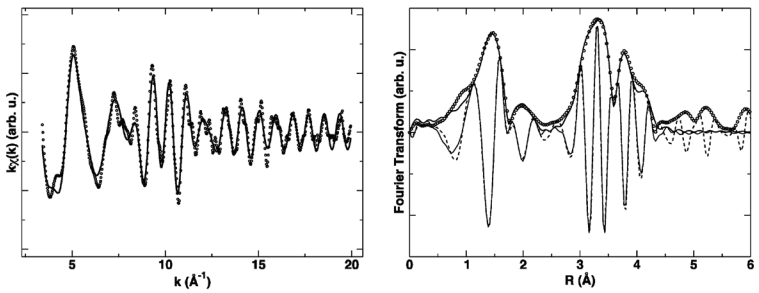

Figure 4.4 A multi-shell fitting in k-space (left) and in R-space (right). The experimental spectra and models are plotted as dots and lines, respectively.

The information extracted from the spectrum is model-dependent, so it is possible to find many models that fit the data, but that do not make any physical sense. For this reason, the data

[7]The interested reader is referred to the documentation of the VIPER free software: http://www.cells.es/Beamlines/CLAESS/software/viper.html.

extraction and modeling are to be conducted in the most economical way, i.e., refining the least number of independent parameters. An oft-quoted figure is the number of independent points from the Nyquist theorem:

$$N_{\text{ind}} \approx \frac{2\Delta k \Delta R}{\pi} \tag{4.6}$$

A cautious strategy is to have at least twice independent points than fitting parameters. During the refinement, some parameters are usually correlated (e.g., N and σ^2 both affect amplitude, MS path length and disorder correlate with those of simple scattering, etc.), so a quantitative assessment of the uncertainties of each parameter of the fitting is difficult. Reasonable estimates of uncertainty are about 0.5 for coordination numbers, 0.01 Å for distances, and 10% for disorder. An example of EXAFS data analysis, reporting explicit uncertainties, is shown in Table 4.1.

Table 4.1 Results derived from the EXAFS analysis of a single coordination shell (the Ge-Ge first shell coordination in amorphous germanium at 77 K)

		a-Ge		
N	—	4.0	±	0.2
R	(Å)	2.468	±	0.005
σ^2	(10^{-3} Å^2)	2.2	±	0.2

Source: Adapted with permission from [5]. Copyrighted by The American Physical Society.

4.1.3 XANES Analysis

Quantitative modeling of XANES data is very difficult for the increasing complexity of the MS model near the absorption edge, and relatively few cases exist in the literature. However, very important qualitative information is extracted easily from near-edge features.

The oxidation state of a metal ion determines the depth of the energy of the core electrons, so that higher oxidation states (higher charge) correspond to higher binding energies, and therefore to the absorption edges being shifted to the right. In many cases, the presence and shape of pre-edge peaks, which are due to transitions between core states and valence states, also

help in identifying the oxidation state (see Fig. 4.5). With the aid of model compounds, comparison between the measured and reference spectra can resolve precisely even slight changes in electronic states [6]. The shape of the absorption edge is also determined by the shape of the first coordination shell, and can be used as a sort of fingerprint: In some cases, pre-edge transitions between bound states may be forbidden in octahedral symmetry and can be used for instance to discriminate between octahedral and tetrahedral coordination.

The broadening of near-edge features increases with E, so that lower-energy edges (typically K-edges of first row transition metals, and L-edges of heavier elements) are more often used in the XANES analysis.

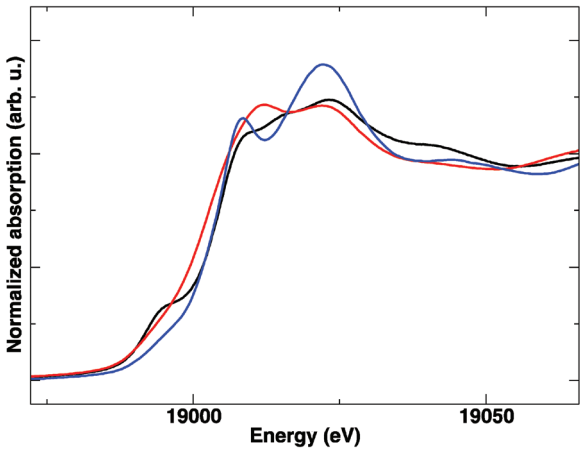

Figure 4.5 Normalized XANES spectra on the Nb K-edge of: NbO_2 (red), Nb_2O_5 (black) and $BaCe_{0.84}Y_{0.1}Nb_{0.06}O_3$ (blue). Both oxidation state and coordination environment have an effect on the near-edge features, and give information on the state of Nb in the perovskite.

4.1.4 XAS Experiments

XAS experiments are performed in dedicated beamlines at synchrotron radiation facilities, which provide a monochromatic, tunable, intense X-ray source. Synchrotrons are large-scale electron storage rings (about 100 m in radius) where electrons are accelerated at a few GeV: The constant acceleration needed to

keep the electron beam on a circular orbit leads to the emission of intense radiation along the horizontal tangent to the orbit. Synchrotron radiation is continuous in the IR-X-ray range, easily collimated in microscopic spots, and it is exceedingly intense if compared to laboratory sources. Even higher brilliance and collimation is achieved with so-called insertion devices, in which the electron orbit is subjected to alternating magnetic fields. A complete introduction to the accelerator physics and to the experimental techniques available with synchrotron radiation can be found in [7].

The most common configurations in XAS experiments are (1) transmission geometry (Fig. 4.6a), in which the absorption coefficient is measured from the intensity of the incoming and transmitted beam through the Beer–Lambert law described in Eq. 4.1; (2) fluorescence geometry (Fig. 4.6b), in which the absorption coefficient is derived indirectly from the intensity of the fluorescence radiation that comes from the sample as a result of the absorption process, I_f. In this case, the absorption coefficient is proportional to I_f/I_0.[8]

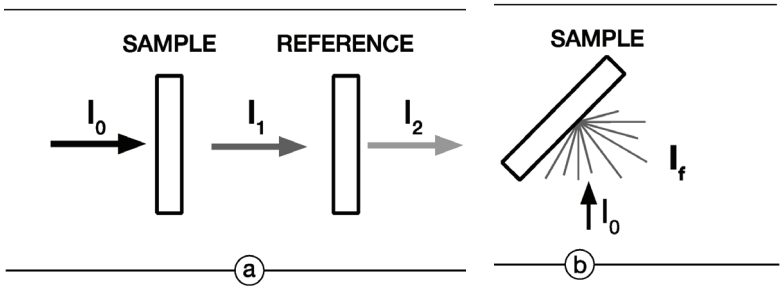

Figure 4.6 (a) Transmission geometry with sample and reference standard; (b) Fluorescence geometry (aerial view), with the sample surface 45° from both the incoming beam and detector.

Transmission geometry, where possible, assures the best signal-to-noise ratio (s/n), fast acquisition and less sources of errors. A usable spectrum can be measured if the absorber is concentrated enough: ideally, the best s/n is achieved with an absorption jump around 1, but reasonably good data can still

[8]Other configurations, less frequently exploited, are possible (e.g., total electron yield, reflection geometry, time-resolved fast measurements).

be collected with a jump of around 0.1. At the same time, the total absorption of the sample, which is due to all the elements present, must not be too high. The optimal total absorption is around 1–2. Higher total absorption can cause systematic errors in the transmitted beam intensity. The total absorption and the absorption edge jump are calculated from the sample composition and weight using tabulated X-ray absorption coefficients.[9] In practice, samples for transmission are prepared as self-supporting pellets by pressing the sample with a suitable dilutant (cellulose or boron nitride are transparent to X-rays), like one does with infrared spectroscopy. To improve homogeneity, the sample can also be suspended in an inert solvent and deposited on a Millipore filter.

Ionization chambers are used as fast and accurate detectors that also let the X-ray beam pass through, so the incident I_0 and transmitted I_1 beam intensity can be measured in a straightforward way. The common setup also involves a reference sample being measured at the same time: the transmitted beam, I_1, acts as an incoming beam, and a third ionization chamber I_2 is used to measure the beam transmitted by the reference. The absorption edge of the reference is then used as an absolute energy reference for all measurements.

If transmission cannot be used, e.g., when the absorber atom is very dilute, and increasing the amount of sample would just make it totally opaque, the sample is tilted 45° from the incoming beam, and the fluorescence radiation is collected by a detector covering a large solid angle about 90° from the incoming beam. Energy-resolving semiconductors are used as detectors, with several elements in parallel to improve the lower detection limit, which can reach about 10^{14} atoms/cm^2. Good samples for fluorescence are either thin and concentrated (e.g., a thin film) or thick and dilute. This minimizes the systematic errors connected with self-absorption of the fluorescence radiation by the sample itself. Fluorescence is typically most suited for higher-energy edges, since the yield of the radiative de-excitation mechanism increases with energy, and the fluorescence peaks are easier to resolve.

[9] *XAFSmass* and *Hephaestus* are freely available via the Internet.

4.2 Solid Oxide Fuel Cells: Materials for Electrolytes and Electrodes

Modern fuel cell technology is based on the assembly of different solid components [8]; a central role is played by the electrolytic membrane, which determines the operative temperature of the device and the overall balance of plant. To date, a good deal of research activity is focused on the improvement of solid-oxide electrolyte materials, which allow to build robust, modular and low-operative-cost plants for energy production. Among solid oxide electrolytes, anionic conductors, performing the transport of O^{2-} anions from cathode to anode, are currently exploited in actual facilities. A scheme of an anion-conduction SOFC is drawn in Fig. 4.7. A mature technology for stationary fuel cell plants is based on yttria-stabilized zirconia (YSZ) electrolytes. The insertion of Y^{3+} in the zirconia matrix has the effect of formation of oxygen vacancies, according to the defect equation:

$$2Zr_{Zr}^{X} + O_{0}^{X} + Y_2O_3 \leftrightarrow 2Y'_{Zr} + V_o^{\cdot\cdot} + 2ZrO_2 \tag{4.7}$$

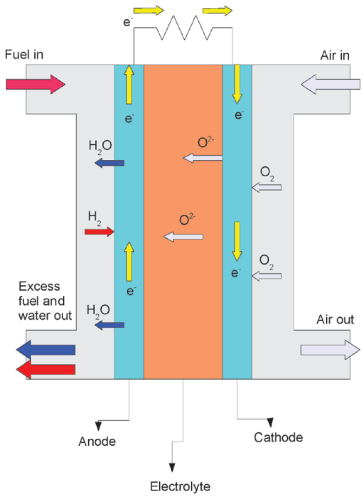

Figure 4.7 Scheme of anion-conduction SOFC.

So, the trivalent dopant insertion improves anion conductivity, by providing empty lattice sites for O^{2-} diffusion paths. Most of the solid oxides with a high anion conductivity crystallize in the

fluorite structure (Fig. 4.8) that is ideally composed of edge-sharing MO_8 cubic boxes. On average, YSZ is cubic (space group *Fm-3m*), while undoped zirconia exhibits a tetragonal distortion of the parent fluorite structure. Energy production plants exploiting YSZ have a high operative temperature (about 1000°C), allowing to work in cogenerative mode and improving the overall process efficiency. On the other hand, such high temperatures require the use of expensive materials and reduce the lifetime of the cell components.

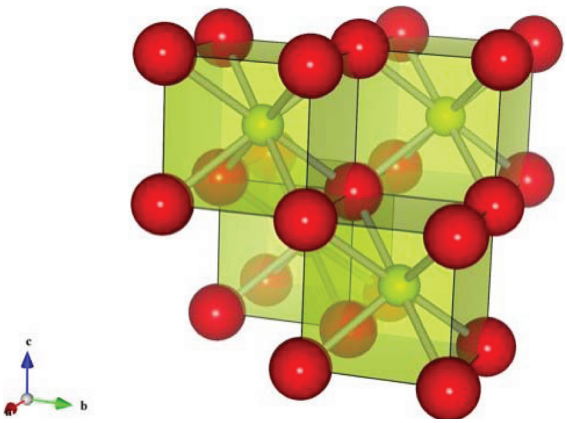

Figure 4.8 The fluorite structure. The cubic oxide cages around the cations are shown (Drawing produced by VESTA [9]).

For anion-conducting electrolytes, the search of alternatives to YSZ has been mainly directed to other fluorites like SDC (samaria-doped ceria) and GDC (gadolinia-doped ceria) [10, 11], and to LSGM ($La_{1-x}Sr_xGa_{1-y}Mg_yO_3$), which has a perovskite structure [12]. The issues concerning the ceria-based electrolytes are focused on the suppression of electronic conduction, that can depend on Ce^{4+} reducibility and, for LSGM, on phase segregation that lowers the grain boundary conductivity.

The electrolyte materials with the highest anionic conductivity, related to δ-Bi_2O_3, are the subject of an intense research activity that aims to stabilize the fluorite structure [13], so far with only partially positive results.

A drawback of anionic conductors, stemming from the simultaneous presence of fuel and reaction products (e.g., water) at the anode compartment, is the necessity of implementing fuel

recirculation to improve the device efficiency. A way to simplify the fuel management is that of using protonic conductors (Fig. 4.9).

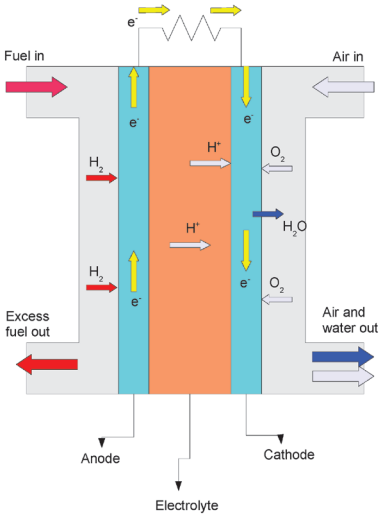

Figure 4.9 Scheme of a proton-conduction SOFC.

To date, the proton-conduction fuel cells that have reached the phase of mature technology are the PEMFC, in which the electrolyte is a polymer membrane, Nafion, or similar materials. The drawback of the PEMFC is the low working temperature (less than 100°C in actual devices), producing easy poisoning of the noble-metal anode catalyst by pollutants such as the carbon monoxide present in the fuel [14].

The consequent request of high-purity (under a few ppm) feeding streams can be overcome by the development of new polymeric materials working at a higher temperature, or to seek for proton conducting ceramics working at definitely higher temperatures [15].

The state-of-the-art proton-conducting ceramics in the temperature range 350–750°C are currently based on strontium and barium cerates and on calcium and barium zirconates [15, 16]. These oxides have a perovskite-type ABO_3 structure, in which the B^{4+} cation lies in an octahedral cage of oxygens; the octahedra share the vertices and the A^{2+} cations are located in the cuboctahedral cavities formed by the network of the octahedral cages (Fig. 4.10).

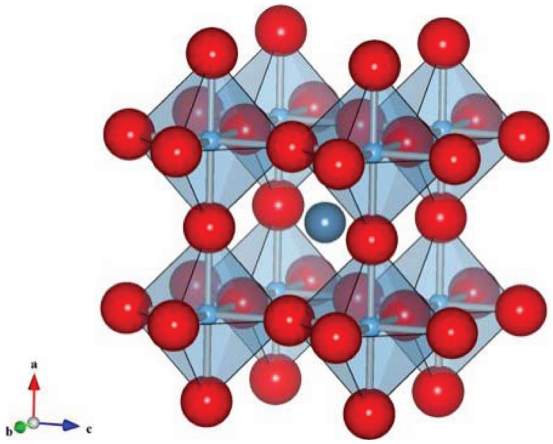

Figure 4.10 ABO_3 perovskite structure. The octahedral oxide cages around the B^{4+} cations are shown. The A cations lie in the cavities formed by the BO_6 octahedra (Drawing produced by VESTA [9]).

In order to introduce protons in the perovskite, the B site is doped with an M trivalent species. Charge neutrality is accomplished by formation of one oxygen vacancy every two M^{3+} cations introduced in the host structure, giving rise to an oxygen-defective solid with formula $AB_{1-x}M_xO_{3-\delta}$. In hydration conditions, an OH^- group is introduced in an anionic vacancy, while a proton H^+ binds to a lattice oxygen. Equations 4.8–4.9 account for the defect equilibrium in barium cerate.

$$2Ce_{Ce}^{X} + O_0^X + Y_2O_3 \leftrightarrow 2Y_{Ce}' + V_0^{\cdot\cdot} + 2CeO_2 \tag{4.8}$$

$$O_0^X + V_0^{\cdot\cdot} + H_2O \leftrightarrow 2OH_0^{\cdot} \tag{4.9}$$

Overall, in the assumption that all the oxygen vacancies are filled, the number of protons introduced in the structure is equal to the number of dopant M^{3+} cations; the mechanism of proton conduction is based on the hopping of proton between neighboring oxygens, assisted by lattice vibrations [17].

The chemical stability of the above-cited cerates with respect to the reaction with acid compounds in the atmosphere, such as CO_2 or SO_2, is quite limited and leads to the decomposition of

the proton conductor. For instance, $BaCeO_3$ reacts with CO_2, producing barium carbonate and cerium oxide. On the other hand, the zirconates have a definitely higher chemical stability, but also a high grain boundary resistivity, likely due to oxide demixing at the needed sintering temperatures and/or reduction of symmetry that affects the probability of proton diffusion paths [18].

These drawbacks of proton-conducting ceramics prevented, so far, the exploitation of these materials in practical devices different from hydrogen sensors. One of the challenges of the chemistry of materials is therefore represented by the development of new ceramics that join high proton conductivity with chemical stability, thus allowing implementation in actual energy production plants.

In the assembly of an FC device, the electrolyte is complemented by the electrode compartments. Electrode SOFC materials accomplish various tasks: (1) provide catalytic fuel oxidation sites at the anode and oxygen reduction at the cathode; (2) transport ionic species to/from the interface with the electrolyte; (3) convey electrons coming from fuel oxidation to the external circuit (anode) and allow their transport to the species to be reduced at the cathode. Moreover, electrode materials should be stable in reaction environment and a good compatibility with the electrolyte, in terms of similar thermal expansion coefficients and absence of diffusion processes leading to the formation of unwanted interface phases, is also needed. The fulfillment of the cell electrochemical reaction needs the contact between the ion conduction, the electron conduction and the gas phases, constituting the so-called triple phase boundary (TPB) [19].

The TPB spatial extent is crucial for the device performance and can be effectively improved by exploiting materials that have mixed ionic-electronic conduction (MIEC). Among the anode materials meeting this requisite, the cermets are composite ceramic-metallic materials whose oxide phase is in charge of ionic transport and electrolyte interface compatibility, while the metal phase provides the catalytic sites and the electronic conduction. However, these materials have the drawback of poor resistance to poisoning, especially when the FC devices are fed with hydrocarbon-containing fuels, and of metal particles sintering [20]. To overcome these problems, in the last years the possibility

was investigated of using mixed oxides encompassing in a single phase all the properties required for anode materials [20, 21]. The issue of mixed ionic-electronic conductivity, beside oxygen reduction activity, was addressed also for cathodes [22]; starting from the perovskite $La_{1-x}Sr_xMnO_3$ (LSM), so far a wide variety of cathode oxides have been formulated and tested in SOFC applications [21].

4.2.1 Case Study 1: Tailoring the Grain Boundary in Nanocrystalline Ceria

The grain boundary is the interfacial, ill-ordered, contact region between differently oriented crystallites of a polycrystalline material. Grain boundary structures are typically present in SOFC electrolyte membranes, whose full-density sintering is necessary in order to prevent leakage of unreacted fuel to the cathode. A TEM micrograph of a full-density YSZ electrolyte is shown in Fig. 4.11.

Taking into account the issue of electrical conduction in ceria and zirconia doped with trivalent species, the grain boundary is characterized by an accumulation of positive charge carriers inducing, by charge compensation, a depletion of carriers of the same sign in the space charge layers adjacent to the grain boundary core [24, 25]. In a typical ceramic anion conductor, e.g., Y- or Yb-doped ceria, the trivalent dopants constitute effective negative defects, while the doubly positively charged oxygen vacancies (Eq. 4.7) are the actual mobile charge carriers. In the sintering process, the negative dopants are mobilized towards the grain boundary core, partially neutralizing the positive potential originated by the excess of oxygen vacancy concentration at the grain boundary core. The still present depletion of positive oxygen vacancies in the adjacent space charge layers is at the origin of the low grain boundary conductivity affecting these solid oxide electrolytes and, similarly, also YSZ. So, a possible way to overcome the lack of grain boundary conductivity in ceria and zirconia-based electrolytes could be that of a suitable modification of the grain boundary composition.

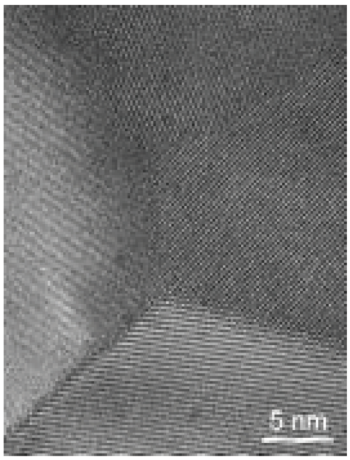

Figure 4.11 High-resolution transmission electron microscopy of grain boundaries in a sample of YSZ with an average grain size of 120 nm. Reprinted from *Prog. Mater. Sci.*, 51, Guo and Waser, Electrical properties of the grain boundaries of oxygen ion conductors: Acceptor-doped zirconia and ceria, pp. 151–210, Copyright 2006, with permission from Elsevier [23].

This hypothesis was examined in a study involving the comparison between homogeneous Y-, Yb-, and Bi-doped ceria electrolytes and the oxides modified by the same heteroatoms but prepared by grain boundary decoration [26]. While the homogeneously doped samples were prepared by coprecipitation, the decoration was achieved by dissolution of the dopant nitrate in water, addition of undoped ceria, drying and final calcination at 450°C. X-ray powder diffraction allowed to demonstrate that both routes produced a single crystalline fluorite phase; some relevant results of the local structure analysis carried out by EXAFS analysis are reported below. Figure 4.12 shows the Fourier-transformed EXAFS spectra of the Y-doped samples, both homogeneous and decorated. The reference Y_2O_3 spectrum confirms the XRD evidence that secondary phases, even if poorly crystallized, are absent. It is also evident by inspection the difference between homogeneously doped and decorated samples, pointing to a different distribution of dopants in the host oxide.

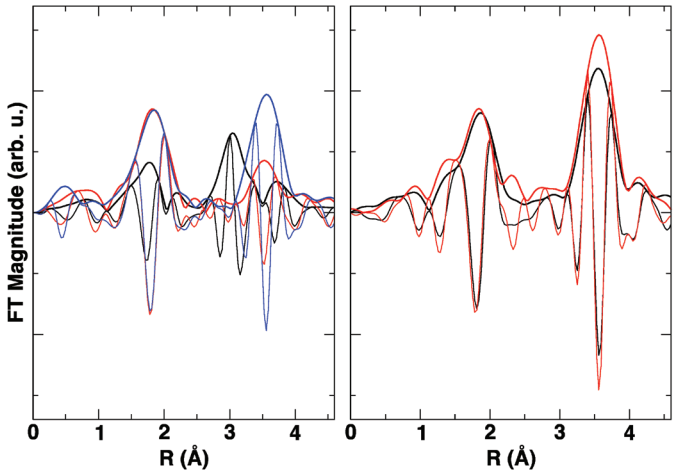

Figure 4.12 FT EXAFS data on the Y K-edge. Left panel: Y_2O_3 (black); Y-decorated powder (red); Y-decorated sintered (blue). Right panel: Y-doped powder (black); Y-doped sintered (red). Thick lines are moduli, thin lines are imaginary parts. Reproduced with permission from *J. Electrochem. Soc.*, 159, B417 (2012). Copyright 2012, The Electrochemical Society [26].

Table 4.2 reports the details of the EXAFS analysis carried out on the sintered homogeneous and decorated YDC samples on both the Ce and Y edges. It seems particularly significative the comparison between the disorder factors: The lower value of $\sigma_{Ce\text{-}O}$ in the decorated sample can be attributed to the grain boundary segregation of dopants and, consequently, to the lesser number of perturbed bulk Ce atoms; on the contrary, the higher σ values on the Y side are assigned to the large variety of different local structures that can accommodate the Y atoms in the perturbed grain boundary region.

Table 4.2 EXAFS analysis of the sintered homogeneously doped and decorated YDC samples

	$R_{Ce\text{-}O}$ (Å)	$\sigma_{Ce\text{-}O}$ (10^{-3} Å^2)	$R_{Y\text{-}O,1}$ (Å)	$R_{Y\text{-}O,2}$ (Å)	$\sigma_{Y\text{-}O}$ (10^{-3} Å^2)	$R_{Y\text{-}Ce}$ (Å)	$\sigma_{Y\text{-}Ce}$ (10^{-3} Å^2)
Homogeneous	2.32	10	2.31	2.46	2.5	3.80	7.1
Decorated	2.33	8.3	2.28	2.40	3.0	3.79	9.3

Source: Adapted with permission from [26]. Copyrighted by The Electrochemical Society.
Note: Uncertainty is on the last digit.

The local structure analysis is coherent with the conductivity data obtained by complex impedance spectroscopy: While homogeneously doped samples shows two clearly distinguishable conductivity contributions, respectively attributed to bulk and grain boundary anion diffusion paths, the decorated samples show a single contribution that, on the basis of the EXAFS analysis, was attributed to the preferential anion diffusion into the heavily doped grain boundary region.

As a final remark, the complementary knowledge achieved about long/short range structure and conductivity in the investigated materials allowed to demonstrate that it is viable to tailor the grain boundary structure and composition of solid oxide electrolytes in order to improve FC performances.

4.2.2 Case Study 2: The Local Structure of δ-Bi_2O_3

Bismuth oxide presents a complex pattern of phase transitions in the range from room temperature up to the melting temperature. The monoclinic α form is stable until 729°C, while the δ form exists between 729 and the melting point at 824°C. On cooling, transitions to the metastable β and γ forms are encountered. The δ-Bi_2O_3 has a oxide-defective fluorite-like structure, with 25% of missing oxide ions; it is the best oxide ion conductor, with a conductivity reaching 1 S/cm at 750°C, but many factors hinder the FC applications, including stability in a wider thermal range, chemical reactivity in reductive environment and low mechanical strength [27]. However, the scientific literature on bismuth oxide-based conductors is considerable, owing to possible applications for oxygen separators and to studies aiming at a deeper insight in the oxide conduction mechanism, eventually leading to the design of new FC materials.

The structure of δ-Bi_2O_3 has been investigated mainly by X-ray and neutron powder diffraction [28]. The long-range analysis showed that the oxide atoms can occupy, beside the regular tetrahedral 8*c* sites of the fluorite structure, also the interstitial 32*f* sites of the *Fm-3m* space group. For undoped Bi_2O_3, the proposed mechanism of oxide diffusion from a tetrahedral occupied site to neighboring empty involves low-energy diffusion paths through the interstitial 32*f* and the octahedral cavity, as shown in Fig. 4.13.

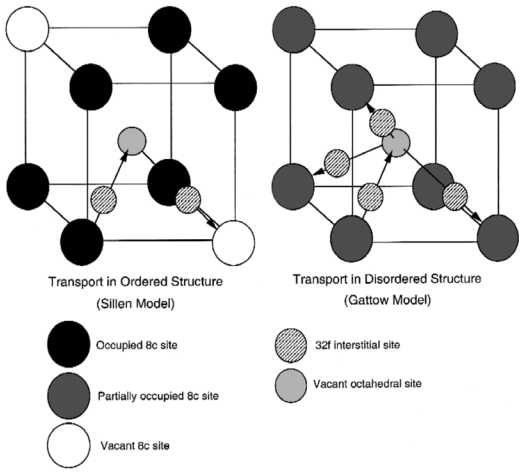

Figure 4.13 Diffusion paths in ordered and disordered δ-Bi_2O_3 through insterstitial 32*f* sites. Reprinted from *Solid State Ionics*, 140, Boyapati et al., Effect of oxygen sublattice ordering on interstitial transport mechanism and conductivity activation energies in phase-stabilized cubic bismuth oxides, pp. 149–160, Copyright 2001, with permission from Elsevier [28].

The slow transition from the disordered to the ordered pattern of oxygen vacancies takes place on cooling below 600°C and involves a remarkable drop of oxide conductivity, due to the reduced probability of finding a suitably oriented diffusion path.

The effect of doping Bi_2O_3 with isovalent or aliovalent cations results in the stabilization to low temperature of the δ phase, at the expense of a loss of oxide conductivity depending on the type and concentration of dopants introduced in the host matrix. To this concern, the best performing stabilized δ-Bi_2O_3 compounds were obtained with a composition $Bi_{12.5}RE_{1.5}ReO_{24.5}$ (RE = La, Nd), with the cations randomly distributed in the 4*a* (0,0,0) and the oxygens partitioned between the 8*c* (0.25,0.25,0.25) and the 32*f* (*x*,*x*,*x*), $x \approx 0.37$, sites of the *Fm*-3*m* space group. Interestingly, the smaller dopants Y and Er have similar *x* value but a conductivity value similar to the Re-free compounds [13]. The cited authors recognized that a detailed analysis of the local environment of cations was necessary, but only partial results, concerning the Er doped compounds, were published. The k^3-weighted FT of the

respective cation L_3 edges (the FT of the Er L_3 edge is shown in Fig. 4.14) did not gave structural information beyond the first shell, leading to the conclusion that the oxide shell around Er and Bi are highly disordered, even if the reported Debye–Waller coefficients (σ^2 = 0.007 Å^2 and σ^2 = 0.006 Å^2, respectively) are not exceedingly high. Further investigation about the local structure of stabilized delta-bismuth oxides seems suitable, also to shed light in the mechanism of oxide diffusion in fluorites that could improve the design of new anion conductors. With this respect, a synergetic complement with simulation approaches, like the ab initio MD study recently reported for $Bi_{1-x}V_xO_{1.5+x}$ [30], can be very useful.

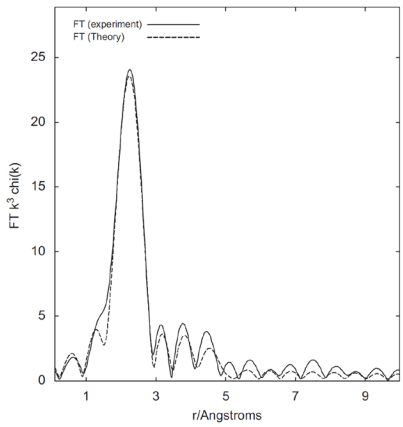

Figure 4.14 Fourier-transformed EXAFS data of the Er L_3-edge of $Bi_{12.5}Er_{1.5}ReO_{24.5}$. Reprinted from *J. Phys. Chem. Solids*, 69, Punn et al., The local environment of cations in $Bi_{12.5}Er_{1.5}ReO_{24.5}$, pp. 2687–2690, Copyright 2008, with permission from Elsevier [29].

4.2.3 Case Study 3: The Role of the Dopant in Proton-Conducting Perovskites

Proton-conducting perovskites (PCP) have a general formula M^{3+}: $A^{2+}B^{4+}O_3$, in which the trivalent M cation substitutes the B cation, and protons are incorporated as described by Eqs. 4.8–4.9. The research activity on PCP, starting in the 1980s, was based on the combination of a wide range of different ABO_3 compounds (mostly $ACeO_3$ cerates and $AZrO_3$ zirconates), and various dopants.

Eventually, all of the proposed compounds presented some chemical, structural, or phase instability that hindered a real-life fuel cell application. A growing interest was then directed at studying the structural mechanisms underlying the shortcomings in chemical stability, and proton mobility. Several techniques (pulsed-field gradient NMR, quasielastic neutron scattering, neutron diffraction and MD simulations) have been used to probe the dynamics of the proton and the structure of the proton binding sites.

In an attempt to give a systematic approach to proton conduction in oxides, Kreuer proposed that "not only a good size matching but also acid/base matching is required in the choice of the acceptor dopant with respect to an optimization of proton mobility" [31]. This proposition was put forward even more openly, on the basis of combined molecular dynamics simulations, hydration thermochemistry, and conductivity experiments, when Y^{3+} was identified as the best possible dopant for $BaZrO_3$, since "the enthalpy of formation of protonic defects is virtually unchanged by the presence of the dopant" [32].

The reported values of proton mobility and activation energy in groups of differently doped perovskites suffer from a lack of consistency, since there is a strong correlation between transport properties and the preparation history of the pellets–especially in zirconates, which are notoriously difficult to sinter. In general, a very large number of impedance spectroscopy studies are available for almost every PCP, while the information gained on their fundamental solid-state chemistry has been relatively low.

An element-selective, local probe like X-ray absorption spectroscopy is ideally suited to investigate the dopant sites in the solid state, while also providing good statistical average (some 10^{18} perovskite unit cells are probed in a XAS experiment). The main results on $BaCeO_3$ and $BaZrO_3$ doped with various trivalent cations are reported below.

Peculiar coordination environments are revealed by EXAFS analysis in various PCP. These arise from the specific interaction of the trivalent dopants with the host oxide. Two cases are especially notable: the YO_6 octahedra in $Ba(Ce,Y)O_3$ are more axially elongated than CeO_6 [33]; the Gd-Ba second coordination shell is distorted and contracted in $Ba(Ce,Gd)O_3$, despite the GdO_6 octahedra are larger than the corresponding CeO_6 [34].

The concept of a fixed ionic radius, widely used to design new compounds, and to derive structure-property relations, was found to be not totally adequate to describe the local coordination environments of host and dopant cations alike. For instance, In^{3+} has a variable size—with In-O bonds stretching from 2.11 to 2.16 Å as a function of the oxide overall composition, adapting its size to the host oxide in both $BaCeO_3$ and $BaZrO_3$ [36, 37].

The case of $BaZrO_3$ doped with Y^{3+} can be described instead as a rigid cation in a rigid host matrix. The dopant retains its ionic radius, thereby expanding the YO_6 octahedra with respect to ZrO_6. The overall cation framework of the parent pure $BaZrO_3$, however, is retained on doping, so that only the anion sublattice (first and third coordination shells) expands around Y^{3+} (as shown in Fig. 4.15), and the cation sublattice (second and fourth shells) is the same around both Y^{3+} and Zr^{4+} [37].

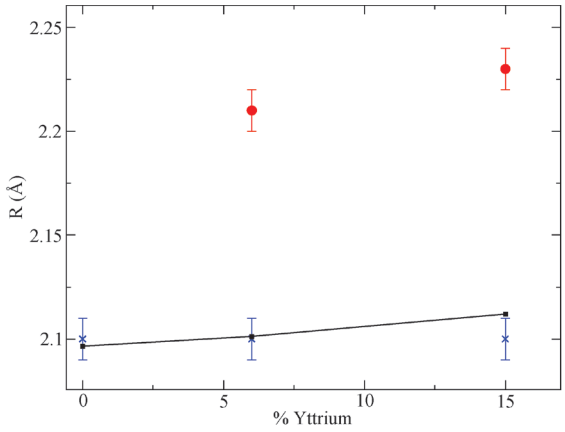

Figure 4.15 First-shell distances around B-site cations in $BaZr_{1-x}Y_xO_3$ as a function of Y content, as determined by X-ray diffraction (average) and X-ray absorption (site-selective). Y-O plotted as red circles, Zr-O as blue crosses, average M-O as black squares. Reprinted with permission from Giannici et al., *Chem. Mater.*, **23**, pp. 2994–3002. Copyright 2011 American Chemical Society [37].

Besides static structural evidence, EXAFS also provided information on the interaction between proton defects and dopant sites: This was achieved by comparing the spectra of the host

and dopant sites in both protonated and deprotonated samples (Fig. 4.16). A neat example is $BaCe_{0.98}Y_{0.02}O_3$, the proton insertion causes only the Y-O, Y-Ba, and Y-Ce bonds to be significantly more disordered, while the corresponding bonds around Ce^{4+} are unaffected. The preferential interaction between defects depends on the particular dopant-host pair: In fact, it is not observed in $BaZr_{0.94}Y_{0.06}O_3$–corroborating the theoretical prediction that there is no difference in basicity between the oxygen sites around Y and Zr, so that the protons bond equally well to either one [32].

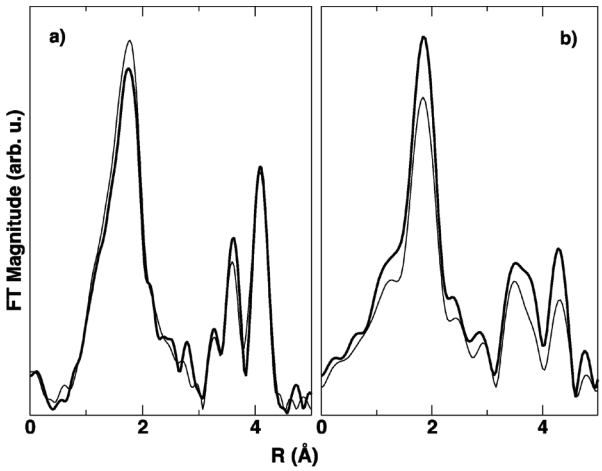

Figure 4.16 The Fourier-transformed EXAFS data of $BaCe_{0.98}Y_{0.02}O_3$ on the Ce K-edge (panel a), and on the Y K-edge (panel b). The thick lines refer to the protonated samples, the thin lines to the deprotonated samples. Data originally presented in Giannici et al., Local environment of barium, cerium and yttrium in yttrium-doped barium cerate, *Solid State Ionics*, 178, pp. 587–591, Copyright 2007 Elsevier [38].

If a trivalent M^{3+} dopant is not completely incorporated in the perovskite oxide, excess M_2O_3 may form at grain boundaries. This is usually poorly crystallized, so that it is often invisible to diffraction techniques, but the distinctive M-M bonds that are typical of M_2O_3 are easily recognized in the EXAFS spectra. For instance, the solubility limit of Y^{3+} in $BaCeO_3$ is around 17%, while nominal compositions around $BaCe_{0.7}Y_{0.3}O_3$ might appear as single-phase with XRD [38]. There is little correlation between

solubility and ionic size: Y^{3+} shows a similar ionic size with Ce^{4+}, while In^{3+} can be inserted in $BaCeO_3$ and $BaZrO_3$ despite a noticeable size mismatch with both Ce^{4+} and Zr^{4+} [35, 36]. In fact, it is worth noting that $BaCeO_3$ and $BaZrO_3$ themselves are miscible despite showing very different symmetry and size: It is clear that the successful insertion of the trivalent dopant depends on chemical parameters that cannot be restricted merely to ionic size.

In conclusion, X-ray absorption spectroscopy provides information on different aspects of the fundamental crystal chemistry behind the doping process in PCP, and on the interaction between lattice defects.

4.2.4 Case Study 4: Electronic Conductivity and Catalytic Activity of LSCM

LSCM ($La_{1-x}Sr_xCr_{1-y}Mn_yO_{3-\delta}$) is a perovskite ABO_3 oxide that combines the high oxidation activity of $LaMnO_3$ and the good stability in reducing environment of $LaCrO_3$. The electronic conduction, obtained by Sr-doping of the A site, is likely related to a small-polaron hopping mechanism. The electronic conduction and the catalytic behavior were investigated by the complementary use of different techniques involving in particular X-ray absorption spectroscopy [39, 40]. In typical LSCM compositions, such as x = 0.1–0.3 and y = 0.5, doping the La site with a bivalent cation involves the introduction of a negative defect, so that charge neutrality is maintained by the formation of positive point defects, e.g., by formation of oxygen vacancies or modification of the oxidation state of the B species. Possible mechanisms are

$$[Sr'_{La}] = 2[V_O^{\bullet\bullet}] + [B_B^{\bullet}] \tag{4.10}$$

or

$$[Sr'_{La}] + [B'_B] = 2[V_O^{\bullet\bullet}] \tag{4.11}$$

In the former case, a p-type conduction takes place, while the latter involves *n*-type.

X-ray absorption spectroscopy is the most suited technique to achieve selective information about the B-site oxidation state, and hence on the electronic conductivity of LSCM. An analysis of

the XANES at the Cr and Mn K-edges of ($La_{1-x}Sr_xCr_{1-y}Mn_yO_{3-\delta}$) (see Fig. 4.17) allowed to show that the valence of Cr does not vary in response to a change in reducing/oxidizing environment. On the contrary, the shift towards higher energies of the Mn K-edge in oxidizing ambient is evidence that Mn changes its oxidation state, likely from 3+ to 4+.

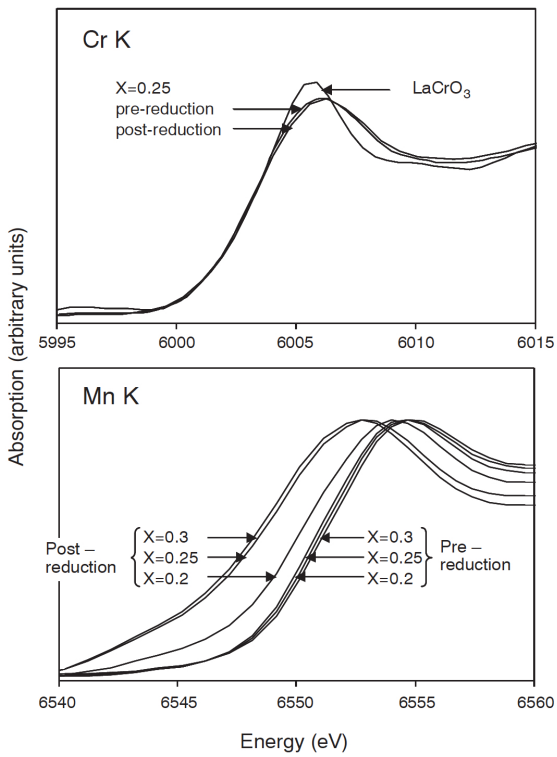

Figure 4.17 The K-edges of Cr and Mn in reducing/oxidizing environment. Reprinted from *Solid State Ionics*, 177, Plint et al., Electronic transport in the novel SOFC anode material $La_{1-x}Sr_xCr_{0.5}Mn_{0.5}O_{3\pm\delta}$, pp. 2005–2008, Copyright 2006, with permission from Elsevier [40].

Then, the defect equilibrium reaction for the Mn oxidation can be expressed as

$$\frac{1}{2}O_2 + V_O^{\cdot\cdot} + 2Mn_{Mn}^{X} \leftrightarrow O_O^{X} + Mn_{Mn}^{\cdot} \tag{4.12}$$

and the electronic conductivity is p-type. Actually, the corresponding equilibrium constant would imply that $[Mn_{Mn}^{\bullet}]$, and hence the electronic conductivity, be dependent on $P_{O2}^{1/4}$, whereas the experimental evidence showed a $P_{O2}^{1/8}$ dependence. This was attributed to a disproportionation of Mn^{3+} in Mn^{2+} and Mn^{4+}, so that the effective electroneutrality condition could be defined, by the complementary X-ray absorption and conductivity experiments, as

$$[Sr_{La}'] + [Mn_{Mn}'] = 2[V_O^{\bullet\bullet}] + [Mn_{Mn}^{\bullet}] \tag{4.13}$$

The EXAFS analysis of LSCM allowed to demonstrate that also the local structure around Cr is not modified on reduction/oxidation, whereas the EXAFS spectra showed a decrease of the oxygen coordination number around Mn. A model of LSCM in reducing environment was then put forth, according to the bidimensional scheme reported in Fig. 4.18.

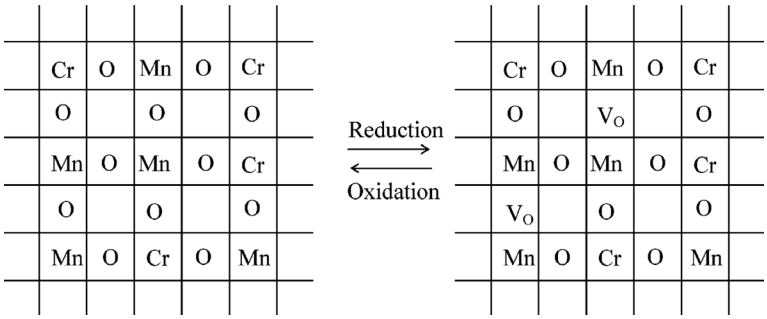

Figure 4.18 Bidimensional scheme of the preferential distribution of $V_O^{\bullet\bullet}$ around Mn. Reprinted with permission from Tao et al., *J. Phys. Chem. B*, **110**, pp. 21771–21776. Copyright 2006 American Chemical Society [39].

The reported case studies show the importance of a local structure analysis in different topics concerning fuel cell solid oxide materials. In summary, the examples, concerning (1) anion-conducting electrolytes, (2) proton-conducting electrolytes, (3) electrolyte grain boundaries and (4) an electrode material, have been chosen as representative of the different compartments of a SOFC device and of the related research issues. Of course, several further examples could be proposed, but we would also outline the fundamental use, in all the reported examples, of complementary experimental techniques allowing, by cross-

analyzing the various pieces of information, to get an overall picture of the investigated materials.

Acknowledgments

We thank Dario Caia for drawing Figs. 4.2 and 4.6 and for help with the page layout.

References

1. Teo, B.-K. (1986). *EXAFS: Basic Principles and Data Analysis* (Springer, Berlin).
2. Stern, E. A. (1987). Theory of EXAFS (Koningsberger, D. C., Prins, R., eds.), in: *X-ray Absorption: Principles, Applications, Techniques of EXAFS, SEXAFS, and XANES*, Chapter 1, Wiley-VCH, Weinheim, pp. 3–53.
3. Rehr, J. J., Albers, R. C. (2000). Theoretical approaches to X-ray absorption fine structure, *Rev. Mod. Phys.*, **72**, 621–892.
4. Bunker, G. (2010). *Introduction to XAFS: A Practical Guide to X-Ray Absorption Fine Structure Spectroscopy* (Cambridge University Press, UK).
5. Dalba, G., Fornasini, P., Grazioli, R., Rocca, F. (1995). Local disorder in crystalline and amorphous germanium, *Phys. Rev. B*, **52**, 11034.
6. Wilke, M., Farges, F., Petit, P.-E., Brown, G. E., Martin, F. (2001). Oxidation state and coordination of Fe in minerals: An Fe K-XANES spectroscopic study, *Am. Mineral.*, **86**, 714–730.
7. Margaritondo, G. (2002). *Elements of Synchrotron Light: For Biology, Chemistry and Medical Research* (Oxford University Press, UK).
8. Larminie, J., Dicks, A. (2002). *Fuel Cell Systems Explained* (John Wiley, Chichester).
9. Momma, K., Izumi, F. (2011). VESTA 3 for three-dimensional visualization of crystal, volumetric and morphology data, *J. Appl. Cryst.*, **44**, 1272–1276.
10. Benamira, M., Ringuedé, A., Albina, V., Vannier, R.-N., Hildebrandt, L., Lagergren, C., Cassir, M. (2011). Gadolinia-doped ceria mixed with alkali carbonates for solid oxide fuel cell applications: I. A thermal, structural and morphological insight, *J. Power Sources*, **196**, 5546–5554.

11. Timurkutluk, B., Timurkutluk, C., Mat, M. D., Kaplan, Y. (2011). Novel structured gadolinium doped ceria based electrolytes for intermediate temperature solid oxide fuel cells, *J. Power Sources,* **196**, 9361–9364.
12. Marrero-López, D., Ruiz-Morales, J. C., Peña-Martínez, J., Martín-Sedeño, M. C., Ramos-Barrado, J. R. (2011). Influence of phase segregation on the bulk and grain boundary conductivity of LSGM electrolytes, *Solid State Ionics,* **186**, 44–52.
13. Punn, R., Feteira, A. M., Sinclair, D. C., Greaves, C. (2006). Enhanced oxide ion conductivity in stabilized δ-Bi_2O_3, *J. Am. Chem. Soc.*, **128**, 15386–15387.
14. Kreuer, K.-D. (2001). On the development of proton conducting polymer membranes for hydrogen and methanol fuel cells, *J. Membr. Sci.*, **185**, 29–39.
15. Iwahara, H., Asakura, Y., Katahira, K., Tanaka, M. (2004). Prospect of hydrogen technology using proton-conducting ceramics, *Solid State Ionics*, **168**, 299–310.
16. Kreuer, K.-D. (2003). Proton-conducting oxides, *Annu. Rev. Mater. Res.*, **33**, 333–359.
17. Kreuer, K.-D., Paddison, S. J., Spohr, E., Schuster, M. (2004). Transport in proton conductors for fuel-cell applications: Simulations, elementary reactions, and phenomenology, *Chem. Rev.*, **104**, 4637–4678.
18. Iguchi, F., Sata, N., Tsurui, T., Yugami, H. (2007). Microstructures and grain boundary conductivity of $BaZr_{1-x}Y_xO_3$ (x = 0.05, 0.10, 0.15) ceramics, *Solid State Ionics*, **178**, 691–695.
19. O'Hayre, R., Barnett, D. M., Prinz, F. B. (2005). The triple phase boundary. A mathematical model and experimental investigations for fuel cells, *J. Electrochem. Soc.*, **152**, A439–A444.
20. McIntosh, S., Gorte, R. J. (2004). Direct hydrocarbon solid oxide fuel cells, *Chem. Rev.*, **104**, 4845–4865.
21. Tsipis, E. V., Kharton, V. V. (2011). Electrode materials and reaction mechanisms in solid oxide fuel cells: A brief review. III. Recent trends and selected methodological aspects, *J. Solid State Electrochem.*, **15**, 1007–1040.
22. McEvoy, A. J. (2001). Materials for high-temperature oxygen reduction in solid oxide fuel cells, *J. Mater. Sci.*, **36**, 1087–1091.
23. Guo, X., Waser, R. (2006). Electrical properties of the grain boundaries of oxygen ion conductors: Acceptor-doped zirconia and ceria, *Prog. Mater. Sci.*, **51**, 151–210.

24. Maier, J. (1986). On the conductivity of polycrystalline materials, *Ber. Bunsenges. Phys. Chem*., **90**, 26–33.

25. Litzelman, S. J., De Souza, R. A., Butz, B., Tuller, H. L., Martin, M., Gerthsen, D. (2009). Heterogeneously doped nanocrystalline ceria films by grain boundary diffusion: Impact on transport properties, *J. Electroceram.*, **22**, 405–415.

26. Lupetin, P., Giannici, F., Gregori, G., Martorana, A., Maier, J. (2012). Effects of grain boundary decoration on the electrical conduction of nanocrystalline CeO_2, *J. Electrochem. Soc.*, **159**, B417–B425.

27. Kharton, V. V., Marques, F. M. B., Atkinson, A. (2004). Transport properties of solid oxide electrolyte ceramics: A brief review, *Solid State Ionics*, **174**, 135– 149.

28. Boyapati, S., Wachsman, E. D., Jiang, N. (2001). Effect of oxygen sublattice ordering on interstitial transport mechanism and conductivity activation energies in phase-stabilized cubic bismuth oxides, *Solid State Ionics*, **140**, 149–160.

29. Punn, R., Gameson, I., Berry, F., Greaves, C. (2008). The local environment of cations in $Bi_{12.5}Er_{1.5}ReO_{24.5}$, *J. Phys Chem. Solids*, **69**, 2687–2690.

30. Kuang, X., Payne, J. L., Johnson, M. R., Radosavljevic Evans, I. (2012). Remarkably high oxide ion conductivity at low temperature in an ordered fluorite-type superstructure, *Angew. Chem. Int. Ed*., **51**, 690–694.

31. Kreuer, K.-D. (1999). Aspects of the formation and mobility of protonic charge carriers and the stability of perovskite-type oxides, *Solid State Ionics*, **125**, 285–302.

32. Kreuer, K.-D., Adams, S., Münch, W., Fuchs, A., Klock, U., Maier, J. (2001). Proton conducting alkaline earth zirconates and titanates for high drain electrochemical applications, *Solid State Ionics*, **145**, 295–306.

33. Longo, A., Giannici, F., Balerna, A., Ingrao, C., Deganello, F., Martorana, A. (2006). Local environment of yttrium in yttrium-doped barium cerate, *Chem. Mater.*, **18**, 5782–5788.

34. Giannici, F., Longo, A., Balerna, A., Martorana, A. (2009). Dopant-host oxide interaction and proton mobility in Gd:$BaCeO_3$, *Chem. Mater.*, **21**, 597–603.

35. Giannici, F., Longo, A., Balerna, A., Kreuer, K.-D., Martorana, A. (2007). Indium doping in barium cerate, *Chem. Mater.*, **19**, 5714–5720.

36. Giannici, F., Longo, A., Balerna, A., Kreuer, K.-D., Martorana, A. (2009). Proton dynamics in in:$BaZrO_3$: Insights on the atomic and electronic structure from X-ray absorption spectroscopy, *Chem. Mater.*, **21**, 2641–2649.

37. Giannici, F., Shirpour, M., Longo, A., Martorana, A., Merkle, R., Maier, J. (2011). Long-range and short-range structure of proton-conducting Y:$BaZrO_3$, *Chem. Mater.*, **23**, 2994–3002.

38. Giannici, F., Longo, A., Deganello, F., Balerna, A., Arico', A. S., Martorana, A. (2007). Local environment of barium, cerium and yttrium in yttrium-doped barium cerate, *Solid State Ionics*, **178**, 587–591.

39. Tao, S., Irvine, J. T. S., Plint, S. M. (2006). Methane oxidation at redox stable fuel cell electrode $La_{0.75}Sr_{0.25}Cr_{0.5}Mn_{0.5}O_{3-\delta}$, *J. Phys. Chem. B*, **110**, 21771–21776.

40. Plint, S. M., Connor, P. A., Tao, S., Irvine, J. T. S. (2006). Electronic transport in the novel SOFC anode material $La_{1-x}Sr_xCr_{0.5}Mn_{0.5}O_{3\pm\delta}$, *Solid State Ionics,* **177**, 2005–2008.